Research article

Linhao Guo, Zelin Hu, Rongqiao Wan, Linyun Long, Tao Li, Jianchang Yan, Yun Lin, Lei Zhang, Wenhui Zhu and Liancheng Wang*

Design of aluminum nitride metalens for broadband ultraviolet incidence routing

https://doi.org/10.1515/nanoph-2018-0151
Received September 14, 2018; revised October 27, 2018; accepted November 11, 2018

Abstract: Ultraviolet (UV) photonics-based device and equipment have various applications in sterilization, military covert communication, medical treatment, nanofabrication, gem identification and so on. The traditional constituent UV components are bulky, inefficient, expensive and easily aging under UV radiation. An all-dielectric metasurface offers a promising way to control the amplitude, polarization and phase of light by engineering the size, shape and distribution of its constituent elements. However, UV components based on all-dielectric metasurfaces are difficult to be realized, due to significant absorption loss for most dielectric materials at the UV region. Here we demonstrate the design of a UV metalens, composed of high-aspect-ratio aluminum nitride nanorods. The in-plane on-axis, off-axis and out-of-plane focusing characteristics have been investigated at representative UVA (375 nm), UVB (308 nm) and UVC (244 nm) wavelengths, respectively. Furthermore, we design UV router for mono-wavelength and multiple wavelengths, that is, guiding UV light to designated different spatial positions. Our work is promising for the development of UV photonic devices and would facilitate the integration and miniaturization of the UV nanophotonics.

***Corresponding author: Liancheng Wang,** State Key Laboratory of High Performance Complex Manufacturing, College of Mechanical and Electrical Engineering, Central South University, Changsha Hunan, 410083, China, e-mail: liancheng_wang@csu.edu.cn, wanglc@semi.ac.cn. https://orcid.org/0000-0002-2100-3089
Linhao Guo, Zelin Hu, Rongqiao Wan, Linyun Long, Tao Li, Lei Zhang and Wenhui Zhu: State Key Laboratory of High Performance Complex Manufacturing, College of Mechanical and Electrical Engineering, Central South University, Changsha Hunan, 410083, China. https://orcid.org/0000-0003-2858-0572 (L. Guo)
Jianchang Yan: Research and Development Center for Semiconductor Lighting, Chinese Academy of Sciences, No. 35A Qinghua East Road, Beijing 100083, China
Yun Lin: Xiangya School of Stomatology, Xiangya Stomatological Hospital, Central South University, Changsha Hunan, 410000, China

Keywords: metalens; ultraviolet spectrum; aluminum nitride; router.

1 Introduction

Metasurfaces have been reported to control amplitude, polarization and phase of light [1–3], and to realize optical functionalities through planar structures, such as metalenses [4–11], meta-holograms [12–20], color filters [21–27], polarizers [2, 28–30] and color imaging [31, 32]. Among these, transmission and reflection metalenses have been investigated through plasmonic or dielectric metasurfaces through Pancharatnam-Berry (PB) phase or phase-encoding (PE) methods in the near-infrared or visible spectrum region, as shown in Table S1 (Section 10 of Supporting Information). A metal plasmon-based metalens has a very low efficiency due to high inherent Joule losses, compared with an all-dielectric metalens with high refractive index, appropriate band gap and low absorption loss. The phase shift and efficiency have to be balanced by the PE method to cover the phase shift from 0 to 2π, while the PB method provides a way to generate an arbitrary phase shift by rotating nanorods with which the efficiency will not be affected.

Ultraviolet (UV) devices based on all-dielectric metasurfaces are few reported due to significant absorption loss for most dielectric materials at the UV region. Furthermore, the application of UV devices is becoming more common in human life, including directional light, sterilizers, laser device and lithography machines. Among these, UV router is a component to filtering and routing UV light to specific positions simultaneously, which is realized by integrating filters, lenses, beam splitters or mirrors in a conventional way. However, the approach is bulky and results in low efficiency, which hinders the development of UV nanophotonics on the trend of miniaturization and high-density integration [33].

For traditional optical UV lenses, phase compensation is achieved from different propagation distances

inside media with different refractive indices, which is called the propagation phase. Yet the PB phase method provides a way to form a spherical wavefront by the geometric phase. Furthermore, it is difficult to converge light into arbitrary positions through traditional lens, yet this can be achieved through a metalens due to its planar configuration and adjustable characteristics: mono-wavelength or multiple-wavelengths UV incidence can be converged into the same position, or arbitrary positions through a rational structure design [34]. Herein, we demonstrate the two-dimensional UV metalens, composed of high-aspect-ratio aluminum nitride (AlN) nanorods. The in-plane on-axis, off-axis and out-of-plane focusing characteristics have been investigated at representative UVA (375 nm), UVB (308 nm) and UVC (244 nm) wavelengths, respectively. Figure 1 overviews the principle and application of a metalens. It sketches in-plane on-axis (A), off-axis (B) and out-of-plane (C) focusing geometrics, whereas the plane and axis denote the incident plane and optical axis, respectively. The schematic of the UV metalens is shown in Figure 1D, with the inset denoting the stereogram of the nanorods. Figure 1E conceptually lists some applications of the metalens: UV router, laser, directional light and lithography. Based on focusing geometrics in Figure 1A–C, we also designed UV router for mono-wavelength and multiple wavelengths, that is, guiding UV light to designated different spatial positions, forming arbitrary patterns, such as line, circular, triangular and quadrants. There are several progresses achieved in this article: (1) metalenses with on-axis, off-axis and out-of-plane focusing configurations have been demonstrated in the UV spectrum by using ultrawide band gap AlN material; (2) UV imaging and router based on the UV metalens are presented. The designed metalens and router are promising for the development of low-cost, lightweight and planar UV nanophotonics.

2 Materials and methods

The band gap of conventional silicon dielectric materials [12, 19, 21] is narrow, resulting in substantial absorption in the UV and even in the visible regions. Titanium oxide [7, 22] and gallium nitride [34] have a relatively large band gap, but not suitable for utilization in the UVB and UVC range. AlN material has been chosen due to its ultrawide band gap (about 6.11 eV, with the absorption edge to be around 202 nm) and a relatively large refractive index (about 2.2) [35–39].

The designed metalens is made up of high-aspect-ratio AlN nanorods in Figure 2A–D, which is equivalent to a half-wave plate, due to the different phase responses to the transverse magnetic and transverse electric incidence [40, 41]. The incident circularly polarized light can be partly converted into its inversed circularly polarized light [4, 42], which has the geometric phase according to the PB phase method [43, 44]. In this article, the incident light is left-hand circularly polarized (LCP) light and the transmitted light is the filtered right-hand circularly polarized (RCP) light. The generated phase shift Φ for a nanorod with rotating angle θ in the case of incident LCP light is $\Phi = 2\theta$, as shown in Figure 2A. Focusing characteristics of the metalens system were investigated with the commercial finite-difference time domain (FDTD) method from the FDTD software package of Lumerical Inc. (Vancouver, BC, Canada). To eliminate boundary effects, perfectly

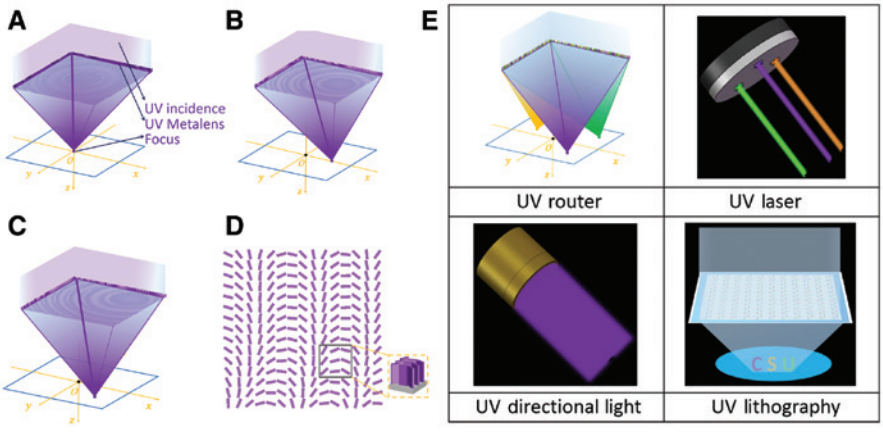

Figure 1: Overviews of the principle and application of a metalens.
Schematics of the UV metalenses with in-plane on-axis (A), off-axis (B) and out-of-plane (C) focusing configurations. The UV metalens is formed by nanorods with varied rotation, which has a ripple-like pattern. (D) Schematic of the UV metalens, with the inset denoting the stereogram of the nanorods. (E) Overview of the applications of the UV metalens.

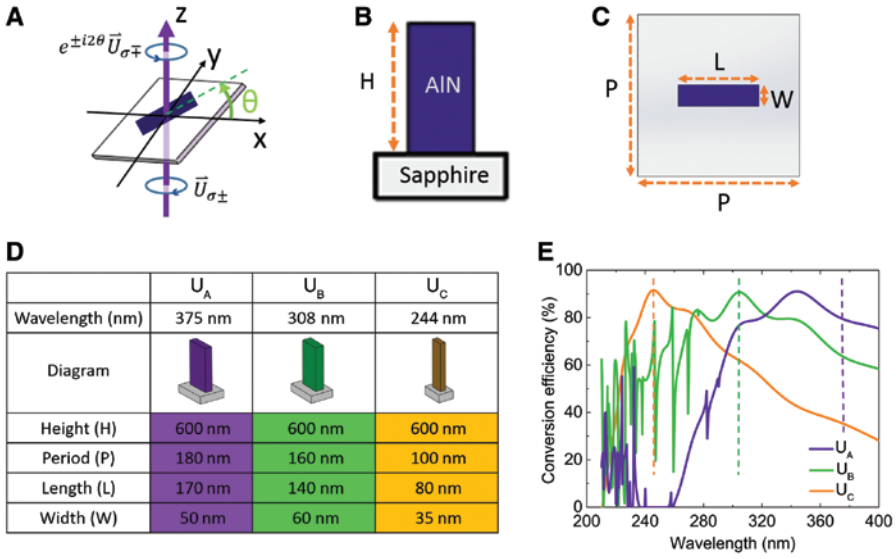

	U_A	U_B	U_C
Wavelength (nm)	375 nm	308 nm	244 nm
Diagram			
Height (H)	600 nm	600 nm	600 nm
Period (P)	180 nm	160 nm	100 nm
Length (L)	170 nm	140 nm	80 nm
Width (W)	50 nm	60 nm	35 nm

Figure 2: The designed metalens is made up of high-aspect-ratio AlN nanorods.
(A) Transmission schematic diagram of circularly polarized light through an AlN nanorod with an orientation angle of θ, with incident circularly polarized light, $\vec{U}_{\sigma\pm}$, transmitted light with opposite circularly polarization, $\vec{U}_{\sigma\mp}$, which is imprinted with a geometrical phase of $e^{\pm i2\theta}$. The left- and right-handed circularly polarized lights are labeled as $\sigma\pm$, respectively. Cross section (B) and top view (C) of the AlN nanorod on the sapphire substrate, with height H, width W, length L and period of the unit cell, P. (D) Geometric dimensions and structure diagrams of three AlN nanorods, marked as UA, UB and UC, respectively. (E) Conversion efficiency between transmitted RCP light and incident LCP light of three AlN structures UA, UB and UC.

matched layers' boundary condition is employed in all the *x*-, *y*- and *z*-directions. The simulation area was discretized using a 3D grid mesh, with a step size of mainly 5 nm in the *x*-, *y*- and *z*-direction.

3 Results and discussion

UVA (375 nm), UVB (308 nm) and UVC (244 nm) are chosen as the representative wavelengths for designing UV router, with the corresponding optimized structures marked as U_A, U_B and U_C, since they have particular applications in gem identification, skin treatments, fabrication of fiber grating, etc. The corresponding geometric dimensions thereof are shown in Figure 2D, with the conversion efficiency estimated to be 79.46%, 89.92% and 91.15% for U_A, U_B and U_C at design wavelengths, respectively. The polarization conversion efficiency is defined as the ratio of the optical power of transmitted inversed circularly polarized light to that of incident light. The interface reflection loss is considered to be around 8% between the air and sapphire substrate, as shown in Figure 2E. There is oscillation for U_B and U_C at a shorter wavelength range, due to the diffraction effect arising from periodic lattices when the effective period of nanorods is more than half of the incident wavelength, which would cause low efficiency at target wavelengths and thus lead to mismatch between the peak of UA conversion efficiency and the target wavelength (375 nm). The UV light is confined in either a resonant or guided manner, which would not affect our design since the working wavelength is on the high-energy side of the diffraction edge [40, 45].

A two-dimensional metalens with in-plane on-axis focusing characteristics at UV-375 nm is shown in Figure 3. For an arbitrary point at (x_l, y_l), the phase shift relative to the center of the metalens is

$$\Phi_{p1}(x_l, y_l) = \frac{2\pi}{\lambda}\left(f - \sqrt{(f^2 + x_l^2 + y_l^2)}\right) \quad (1)$$

where x_l and y_l are coordinates of a nanorod in the metalens, λ is the wavelength of incident light and f is the focal length, set to be 10 μm. According to the PB phase method, the phase shift generated by the nanorod in the (x_l, y_l) position of the metalens surface is

$$\Phi_{m1}(x_l, y_l) = 2\theta_{l1}(x_l, y_l) \quad (2)$$

where $\theta_{l1}(x_l, y_l)$ is the rotating angle of the nanorod in the (x_l, y_l) position. Thus, the metalens would converge light on the designated focal spot when

$$\Phi_{m1}(x_l, y_l) = \Phi_{p1}(x_l, y_l) \quad (3)$$

That is,

$$\theta_{l1}(x_l, y_l) = \frac{\pi}{\lambda}\left(f - \sqrt{f^2 + x_l^2 + y_l^2}\right) \quad (4)$$

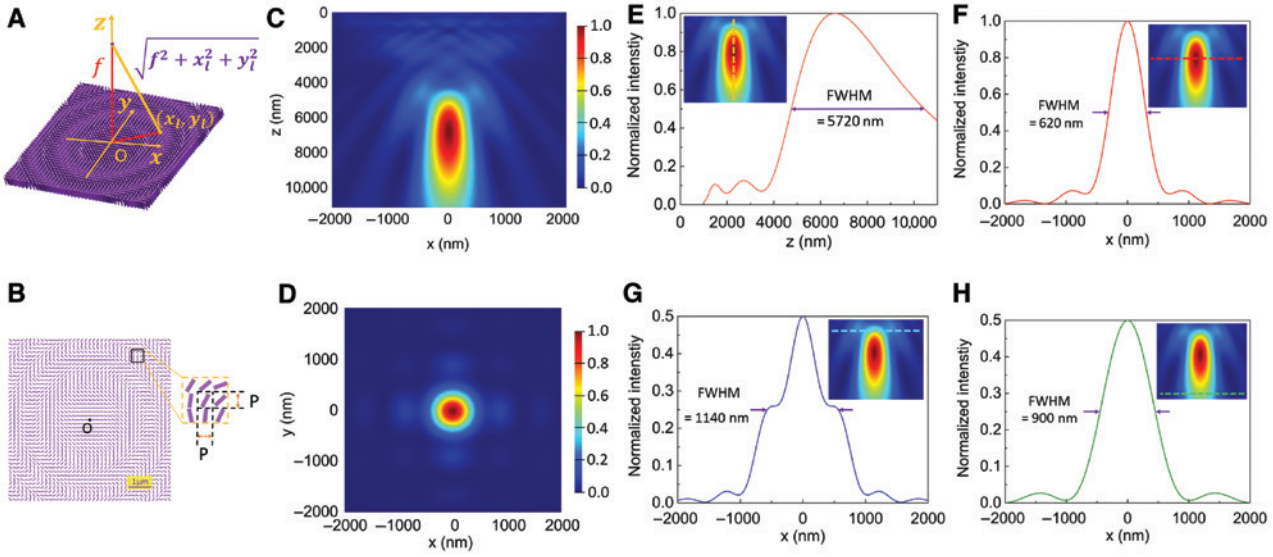

Figure 3: In-plane on-axis focusing characteristics for LCP incidence at UV-375 nm wavelength.
(A) Schematic diagram of in-plane on-axis focusing configuration, consisting of an AlN nanorod array, with rotation of different angles. (B) Top view of the metalens; (C) normalized RCP light intensity distribution at the *x*-*z* section; (D) normalized RCP light intensity distribution at the *x*-*y* section at $z = 6.62$ μm. Normalized intensity profile for the focus spot (E) along the *z*-axis, at $x = 0$, with the peak located at $z = 6.62$ μm; (F) along the *x*-axis, at $z = 6.62$ μm, (G) along the *x*-axis at $z = 4.74$ μm and (H) $z = 10.46$ μm. The size of the metalens is 4 μm × 4 μm, containing 23 × 23 AlN nanorods in total. The NA is 0.196. The top surface is located at $z = 0$. The insets inside (E)–(H) are the enlarged view of the focal spot in (C), where the colored lines denote the position of the data extracted from the focal spot.

According to Eq. (4), the rotating angle of all the nanorods is determined at every position, as shown in Figure 3B. The metalens has a ripple-like pattern, with the center located at the projection position of the focus on the *x*-*y* plane, as shown in Figure 3A and B. The beam intensity profiles in the *x*-*z* cross-section are shown in Figure 3C, where the transmitted beams are converged into a focus spot at $(x, y) = (0, 0)$. The intensity distribution of the focal spot at the focal plane is shown in Figure 3D, exhibiting a symmetric, bright and small spot. The intensity distribution of the focal spot along the *z*-axis shows a peak at $z = 6.62$ μm and full width at half-maximum (FWHM) to be 5.72 μm in Figure 3E. The practical focal length (6.62 μm) is less than the calculated value (10 μm). The practical focusing position is the coordinate point of maximum values of light intensity in the propagating space, which is obtained by data analysis of simulation results. The FWHM of intensity distribution of the focal spot section along the *x*-axis are 620, 1140 and 900 nm at $z = 6.62$ μm (the center of the focus spot), $z = 4.74$ μm (intensity drop to half of the focus spot) and $z = 10.46$ μm (intensity drop to half of the focus spot), as shown in Figure 3F–H, respectively. The in-plane on-axis focusing efficiency is 47.1%, which is defined as the ratio of the optical power in the focal spot area (circle of radius 2 × FWHM spanning the center of the focal spot) to the optical power of the incident beam. The in-plane on-axis focusing characteristics at UV-244 nm and UV-308 nm wavelengths are shown in Figures S1 and S4 (Supporting Information), respectively.

The in-plane off-axis focusing characteristics of the two-dimensional metalens are shown in Figure 4. Similarly, the rotating angle of the nanorod is determined to be

$$\theta_{l2}(x_l, y_l) = \frac{\pi}{\lambda}\left(f - \sqrt{f^2 + (x_l - x_f)^2 + y_l^2}\right) \tag{5}$$

where $\theta_{l2}(x_l, y_l)$ is the rotating angle of the nanorod in the (x_l, y_l) position, x_f is the *x* coordinate of the focusing spot. According to Eq. (5), the nanorods have a rotating angle of almost zero at $(x, y) = (x_f, 0)$, as shown in Figure 4B. Figure 4A and B sketches the in-plane off-axis focusing configuration and the unit of the metalens. The beam intensity profile in the *x*-*z* cross-section is shown in Figure 4C, where the transmitted beam is converged into a focus spot in the *x*-*z* plane, away from the *z*-axis. The focus is located at $x = 0.71$ μm and $z = 6.109$ μm. The intensity distribution of the focal spot section at the focal plane has a symmetric, bright and small spot at $(x, y) = (x_f, 0)$, as shown in Figure 4D. The beam intensity profiles in the *y*-*z* cross-section at $x = 0.71$ μm are shown in Figure 4E, where the transmitted beams are converged at $y = 0$. The intensity distribution of the focal spot along the *z*-axis shows a peak at $z = 6.109$ μm in Figure 4F, where the parameter *f* is set to be 10 μm and x_f is set to be 1 μm. The position

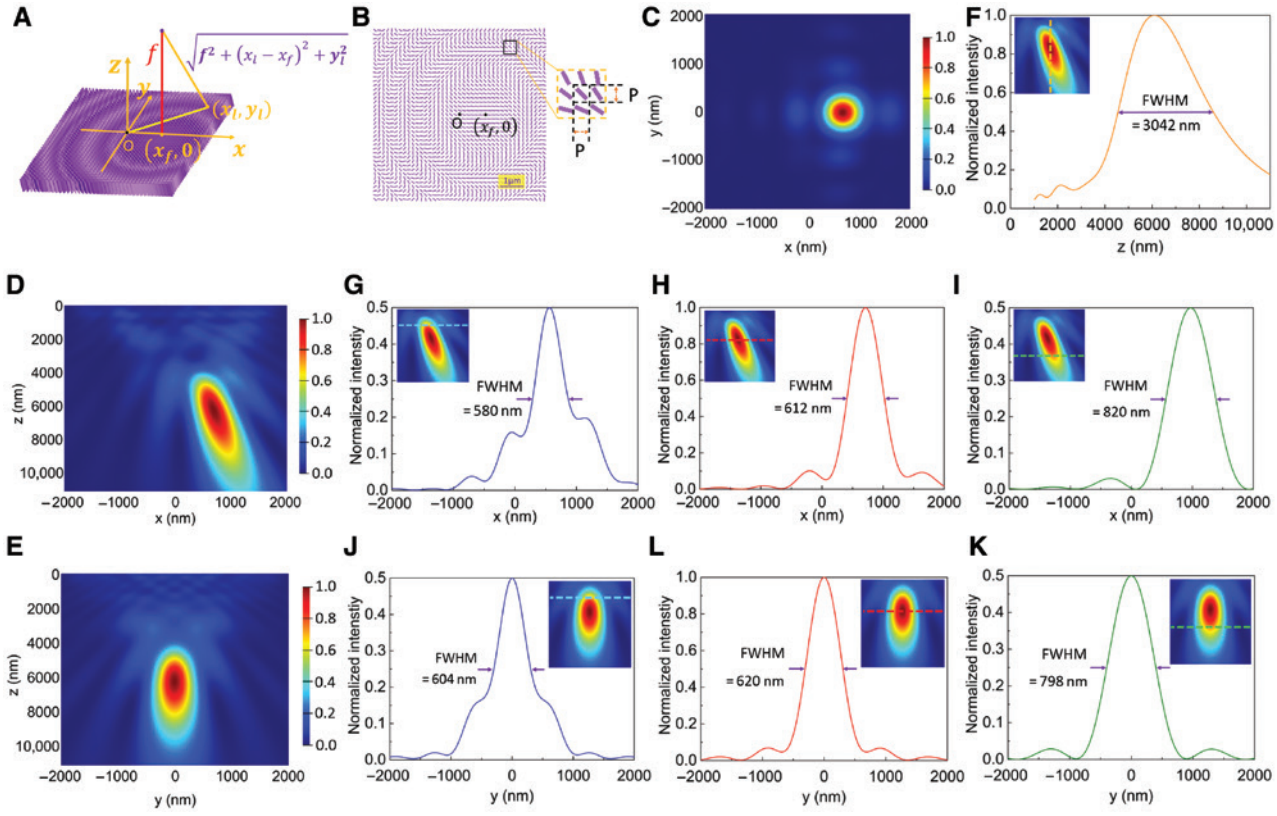

Figure 4: The in-plane off-axis focusing characteristics of the two-dimensional metalens.
In-plane off-axis focusing characteristics for LCP incidence at UV-375 nm: (A) schematic diagram of the in-plane off-axis focusing configuration, consisting of a two-dimensional array of AlN nanorods in the *x*-*y* plane, with different angles as calculated according to Eq. (5). (B) Top view of the metalens. Normalized RCP light intensity distribution across (C) the *x*-*y* section at $z=6.109$ μm, (D) the *x*-*z* section, at $y=0$, (E) *y*-*z* section, at $x=0.71$ μm. (F) Normalized intensity profile along the *z*-axis, at $x=0.71$ μm and $y=0$, with the peak located at $z=6.109$ μm. (G–I) Normalized intensity profile along the *x*-axis, at $z=4.562$ μm, $z=6.109$ μm and $z=8.604$ μm, respectively. (J–L) Normalized intensity profile along the *y*-axis, at $z=4.562$ μm, $z=6.109$ μm and $z=8.604$ μm, respectively. The two-dimensional array has the size of 4 μm × 4 μm, which means that there are 23 × 23 AlN nanorods in total. The NA is 0.196. The top surface of the metalens is located at $z=0$. The insets of (F)–(I) and (J)–(L) are the enlarged view of the focal spot in (C) and (E), respectively, where the colored lines denote the position of the data extracted from the focal spot.

of the focus deviates from the calculated value and tends to be close to the metalens surface in the *z* direction. The FWHM of the plot in Figure 4F are located at $z=4.562$ μm and $z=8.604$ μm at each side. The intensity distribution of the focal spot section along the *x*-axis at $z=6.109$ μm, $z=4.562$ μm and $z=8.604$ μm has a peak near $x=x_f$, as shown in Figure 4G–I, with the FWHM of 612, 580 and 820 nm, respectively. And the intensity distribution of the focal spot section along the *y*-axis at $z=6.109$ μm, $z=4.562$ μm and $z=8.604$ μm has a peak at the center, as shown in Figure 4J–L, with the FWHM of 620, 604 and 798 nm, respectively. The in-plane off-axis focusing efficiency is 45.82%. The in-plane off-axis focusing characteristics at UV-244 nm and UV-308 nm wavelengths are shown in Figures S2 and S5 (Supporting Information), respectively.

A two-dimensional metalens with out-of-plane focusing characteristics at UV-375 nm is shown in Figure 5. However, the rotating angle of the nanorod in the two-dimensional out-of-plane metalens is

$$\theta_{l3}(x_l, y_l) = \frac{\pi}{\lambda}\left(f - \sqrt{f^2 + (x_l - x_f)^2 + (y_l - y_f)^2}\right) \quad (6)$$

where x_f and y_f are the *x* and *y* coordinate of the focus, respectively. Figure 5A and B sketches the out-of-plane focusing setup and the unit of the metalens. The beam intensity profiles in the *x*-*z* cross-section at $y=0.87$ μm and in the *y*-*z* cross-section at $x=0.59$ μm are shown in Figure 5C and E, respectively. The transmitted beam is converged away from the *z*-axis, and out of *x*-*z* and *y*-*z* plane. The focus is located at $(x, y, z)=(0.59, 0.87, 6.209)$ μm. The intensity distribution of the focal spot section at the focal plane has a symmetric, bright and small spot, as shown in Figure 5D. The intensity distribution of the focal spot section along the *z*-axis has a peak at $z=6.109$ μm, as shown in Figure 5F, where the parameter *f* is set to be

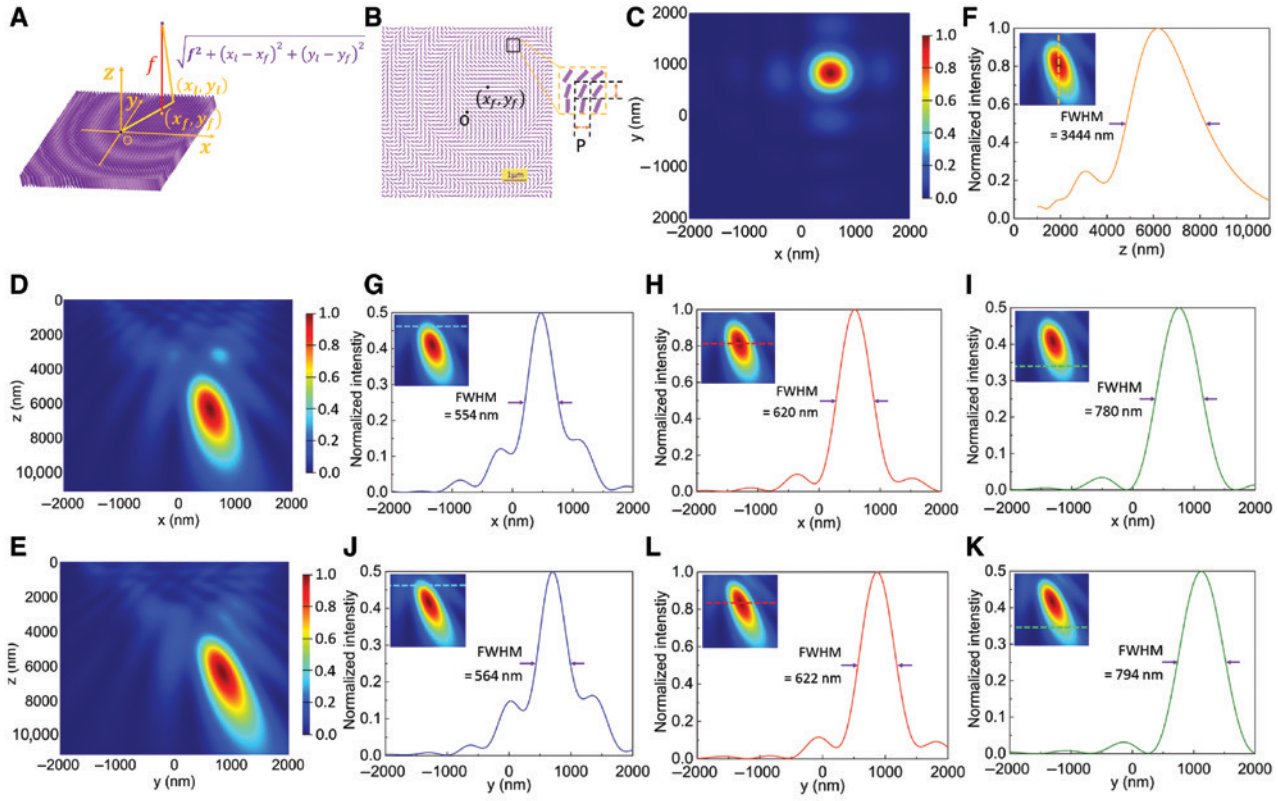

Figure 5: Out-of-plane focusing characteristics at UV-375 nm wavelength.
(A) Schematic diagram of the focusing configuration, consisting of a two-dimensional array of AlN nanorods in the *x*-*y* plane, with different rotation angles as calculated according to Eq. (6). (B) Top view of the metalens, with unit cells of a fixed period equal to the dimension of the nanorods. Normalized RCP light intensity distribution across (C) the *x*-*y* section at $z = 6.209$ μm, (D) the *x*-*z* section, at $y = 0.87$ μm and (E) *y*-*z* section, at $x = 0.59$ μm. (F) Normalized intensity profile along the *z*-axis, at $x = 0.59$ μm and $y = 0.87$ μm, with the peak located at $z = 6.209$ μm. (G–I) Normalized intensity profile along the *x*-axis, at $z = 4.811$ μm, $z = 6.209$ μm and $z = 8.255$ μm, respectively. (J–L) Normalized intensity profile along the *y*-axis, at $z = 4.811$ μm, $z = 6.209$ μm and $z = 8.255$ μm, respectively. The two-dimensional array has the size of 4 μm × 4 μm, which means that there are 23 × 23 AlN nanorods in total. The NA is 0.196. The top surface of the metalens is located at $z = 0$. The insets of (F)–(I) and (J)–(L) are the enlarged view of the focal spot in (D) and (E), respectively, where the colored lines denote the position of the data extracted from the focal spot.

10 μm and x_f and y_f are set to be 0.8 and 1.2 μm, respectively. The FWHM of the plot in Figure 5F are located at $z = 4.811$ and $z = 8.255$ μm at each side. The intensity distribution of the focal spot section along the *x*-axis at $y = 0.87$ μm, and $z = 6.209$ μm, $z = 4.811$ μm and $z = 8.255$ μm has a peak near $x = x_f$, as shown in Figure 5G–I, with the FWHM of 620, 554 and 780 nm, respectively. And the intensity distribution of the focal spot section along the *y*-axis at $x = 0.59$ μm, and $z = 6.109$ μm, $z = 4.562$ μm and $z = 8.604$ μm has a peak near $y = y_f$, as shown in Figure 5J–L, with the FWHM of 622, 564 and 794 nm, respectively. The out-of-plane focusing efficiency is 44.96%. The out-of-plane focusing characteristics at UV-244 nm and UV-308 nm wavelengths are shown in Figures S3 and S6 (Supporting Information), respectively.

The design metalens can also converge light of mono-wavelength incidence into more than one position and multiple wavelengths incidence into different positions, rendering the capability of metalens for light routing. We first design a metalens to route mono-wavelength UV incidence into a line (different polar angles and the same azimuth angle) and circular pattern (different azimuth angles and the same polar angle). Light can be converged into the origin (point 0), positive and negative axes (points 1, 3, 5 and 7) as well as four quadrants (points 2, 4, 6 and 8), with designed hybrid single UV metalens, as shown in Figure 6A–C. The unit cell of light router-LR1 consists of nine AlN nanorods, which is responsible for routing light to the corresponding nine different focusing points, as shown in Figure 6A. Figure 6B shows a circle pattern with one point in the center and eight points distributing uniformly on the circle. The intensity distribution of the nine focal spots at the focal plane is shown in Figure 6C. In the

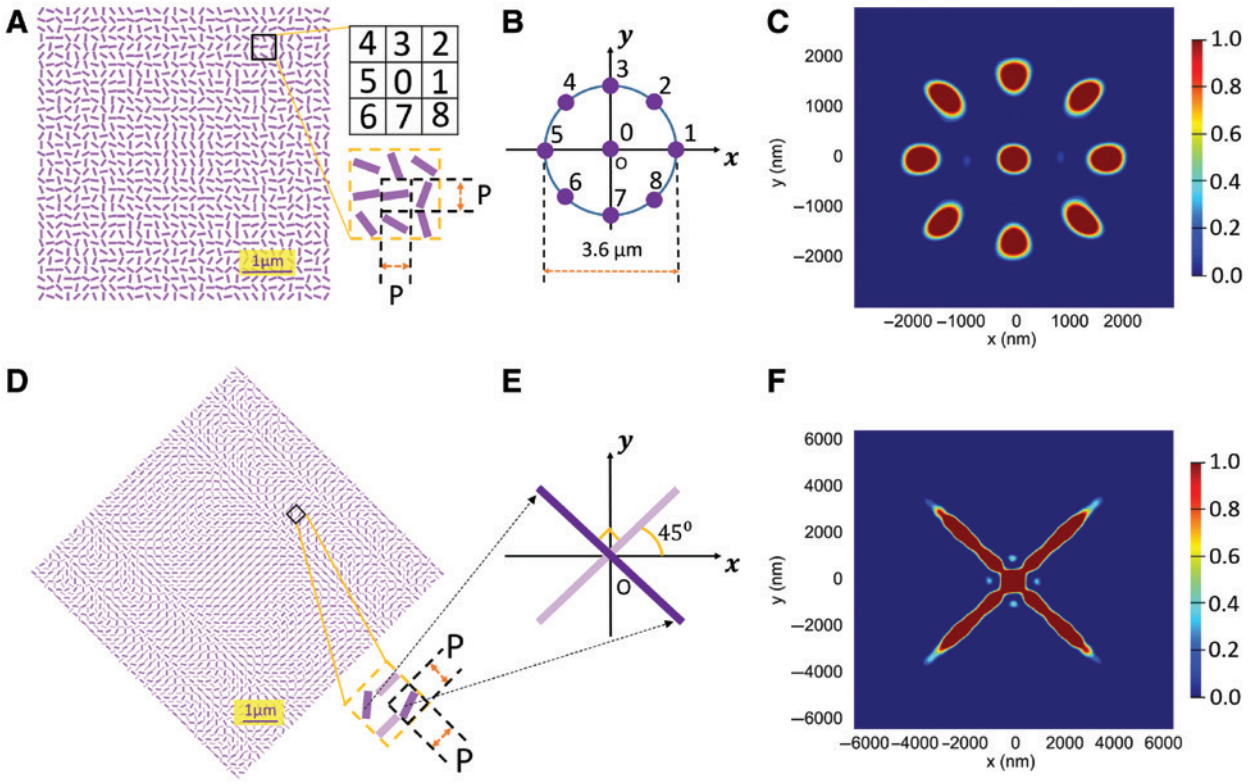

Figure 6: Light routers for mono-wavelength at UV-375 nm.
(A) Top view of light router-LR1, with unit cells consisting of nine AlN nanorods, denoted as UA. The unit cell has a fixed period of 3P = 0.54 μm. The nine nanorods in different positions are marked from 0 to 8. (B) Routing positions of metalens-LR1 in *x*-*y* coordinates. The center of the circle is located at the origin O, with the diameter of 3.6 μm. The figures correspond to the using nanorods as shown in (A). (C) Normalized RCP light intensity distribution of the *x*-*y* section at *z* = 10 μm. (D) Top view of light router-LR2, with unit cells consisting of four AlN nanorods of structure UA. The unit cell has a fixed period of 2P = 0.36 μm. The nanorods used for different lines are marked as deep purple and light purple. (E) Routing angles of the lines of LR2 in *x*-*y* coordinates. The center of the lines is located at the origin O, with the length of 9 μm. Colors of two lines correspond to the using nanorods, as shown in (D). The two lines form an angle of 90° with one of them forming an angle of 45° with the *x*-axis. (F) Normalized RCP light intensity distribution of the *x*-*y* section at *z* = 10 μm. The two-dimensional arrays of LR1 and LR2 have the sizes of 5.94 μm × 5.94 μm and 9 μm × 9 μm, respectively, which means that there are 11 × 11 and 25 × 25 AlN unit cells in total for LR1 and LR2, respectively. The top surface of LR1 and LR2 is located at *z* = 0.

same way, light can also be routed to lines with different polar angles with UV metalens, as shown in Figure 6D–F. The unit cell of light router-LR2 consists of four AlN nanorods, to form two lines with different rotating angles, as shown in Figure 6D. The focusing angle of the lines is shown in Figure 6E, which forms a cross with two lines forming an angle of 90°. The intensity distribution of the two focal lines at the focal plane is shown in Figure 6F, which is like a cross with symmetric shape. The mechanism for imaging of lines is that multiple points generate a line, because the spacing between adjacent points and the size of the building blocks are close to the FWHM of the focal spots, and routing of mono-wavelength light provides a way for imaging of cross line-shape light, both of which need appropriate arrangement of nanorods on the metalens (see Section 8 of Supporting Information). With the capability to tune the polar, azimuth angle and radius, principally we can design a metalens to routing the UV incidence into any arbitrary pattern.

We further demonstrate metalens for multiple UV incidence routing. UV router for UVA (375 nm), UVB (308 nm) and UVC (244 nm) wavelengths is shown in Figure 7. The light router-LR3 is hybridized by various structures of AlN nanorods. The three wavelength incidences are routed into four positions forming a 2-μm-size square, as the Bayer pattern arranged in the color image sensor chips [46]. UV 244, 308 and 375 nm incidence is routed to $(x, y) = (-1\ \mu m, 1\ \mu m)$, $(1\ \mu m, 1\ \mu m)$ and $(-1\ \mu m, -1\ \mu m)$ and $(1\ \mu m, -1\ \mu m)$, respectively, as shown in Figure 7B and C. The unit cell of LR3 consists of 16 AlN nanorods, as shown in Figure 7A. After multiple optimizations, the quantity ratio of UA, UB and UC is chosen to be 2:4:10 (see Section 9 of Supporting Information). The intensity distribution of the four focal spots at the focal plane is shown in Figure 7C, where

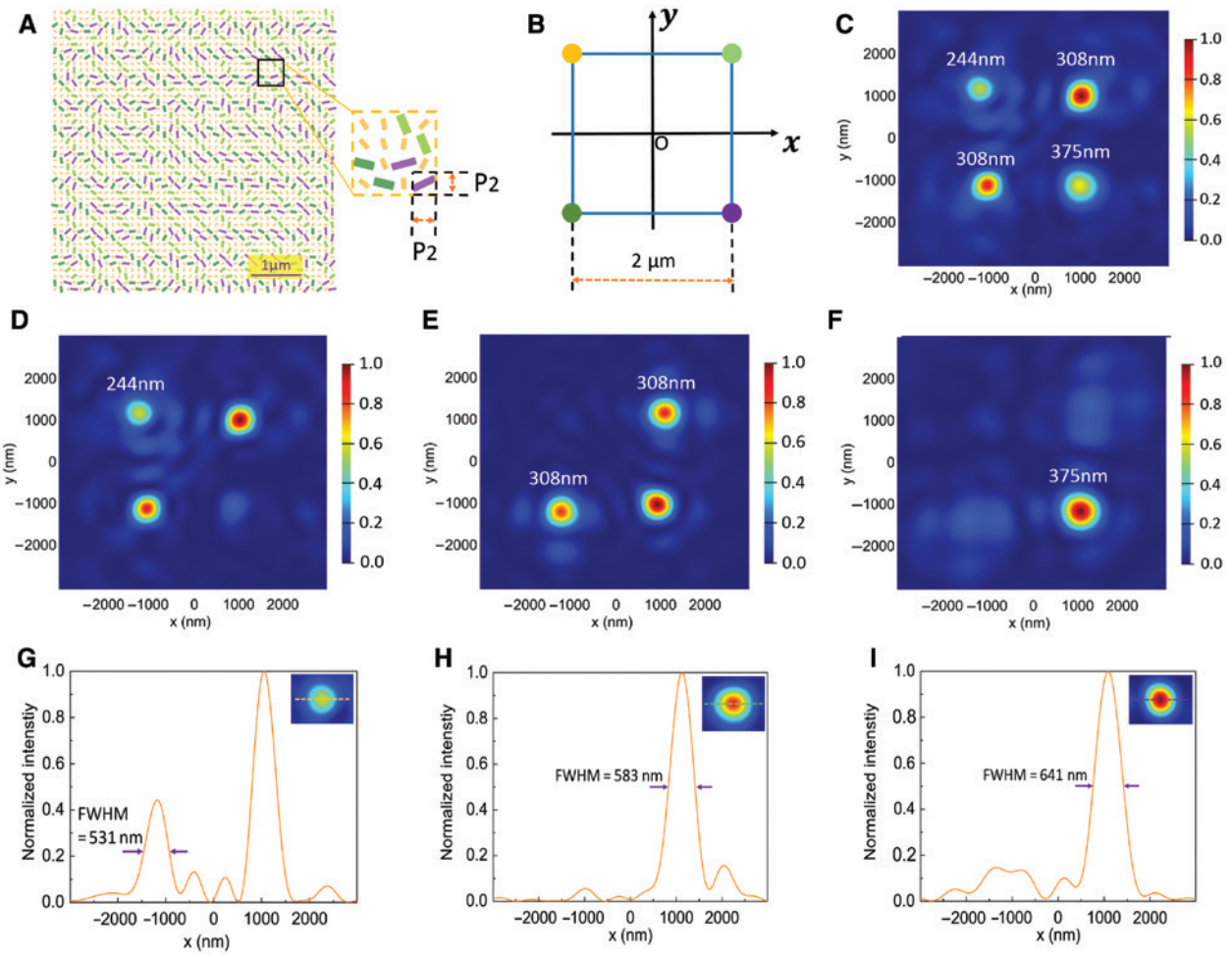

Figure 7: UV router for multiple UV wavelengths at 244, 308 and 375 nm, where the incidences are routed into four positions forming a square.

(A) Top view of light router-LR3, with unit cells consisting of 16 nanorods of structures as shown in Figure 2D, where the quantity ratio of UA, UB and UC is 2:4:10, and two routing positions for UV-308 nm wavelength are distinguished by bottle green and light green colors. The unit cell has a fixed period of 4P2 = 0.54 μm. (B) Routing positions of LR3 in *x*-*y* coordinates for UV-244, 308 and 375 nm wavelengths, with yellow, green and purple colors, respectively, corresponding to the applied structures UA, UB and UC. The center of the square is located at the origin O, with the side length of 2 μm. (C) Routing results of LR3, with incidence of UV-244, 308 and 375 nm wavelengths. (D–F) Routing results of LR3, with incidence of single UV-244, 308 and 375 nm wavelengths, respectively. (G–I) Normalized intensity profiles along the *x*-axis for the focal spot as shown in (D)–(F), respectively. The routing plane is located at $z = 10$ μm. The two-dimensional array has the size of 5.985 μm × 5.985 μm, which means that there are 11 × 11 AlN unit cells in total for LR3. The top surface of LR3 is located at $z = 0$. The insets inside (G)–(I) are the enlarged view of the focal spot in (D)–(F), respectively, where the colored lines denote the position of the data extracted from the focal spot.

LR3 is illuminated with light of UV-244, 308 and 375 nm wavelengths simultaneously. The intensity distribution of the single focal spots at the focal plane is shown in Figure 7D–F, where LR3 is illuminated with light of single wavelength of UV-244, 308 and 375 nm, respectively. The intensity distribution of the focal spot section along the *x*-axis has a peak near the design position for incidence of UV-244, 308 and 375 nm wavelength, as shown in Figure 7G–I, with the FWHM of 620, 554 and 780 nm, respectively. The routing efficiencies for incidence of UV-244, 308 and 375 nm wavelengths are 12.4% (244 nm), 18.6% (first quadrant), 18.0% (third quadrant) and 7.17% (375 nm), respectively. The efficiency for the designed UV metalenses is about 46%, while it is reduced to be lower than 20% for UV routing design. The reduction of efficiency for UV routing is attributed to the region segmentation of the metasurface for different incidences, which leads to different occupancies of different building blocks, while the UV metalenses have the whole metasurface occupied with the same building blocks for single incidence.

The focusing efficiencies for the UV-375 nm metalenses with on-axis, and in-plane, off-axis and out-of-plane focusing characteristics are 47.1%, 45.8% and 44.9%, respectively. The length of practical focusing (i.e. the position of maximum intensity) is smaller than the calculated focal length. The practical focusing position (i.e. the position of the maximum intensity) is therefore closer to the metalens surface than the designed focusing positions for the on-axis metalens and closer to the metalens surface and the z-axis for off-axis and out-of-plane metalens, as shown in Figure S11 (Supporting Information). The reasons for this deviation is that the convergence effect of the design metalens is realized by using the discrete unit cells for approximating the continuous phase shift, where the discrete phase shift between adjacent rings composed of nanorods should be considered for the focusing result, and incident wavelength, period of building blocks and dimensions of metalens are the affecting factors of the practical focal length (Section 12 of Supporting Information). This focusing position deviation can be reduced by increasing the period of building blocks and dimensions of the metalens. Based on the results of line and circular pattern routing, it is reasonable to argue that more complicated and arbitrary patterns can be achieved through a rational design. Thus, the UV metalens can have potential application in UV imaging and UV lithography. The designed incidence (e.g. 244 nm) is routed to the designed focusing position for other wavelength (e.g. 308 nm), as shown in Figure 7D and E, due to the crosstalk effect between the incidence of different wavelengths. The overlapped conversion spectrum of different building blocks and the dispersion effect for different incidences are the main reasons for crosstalk, which is further discussed in Section 11 of Supporting Information. It is difficult to totally eliminate the crosstalk effect due to the dispersion effect, whereas it can be reduced by decreasing the overlapped region of different building blocks. This can be achieved by further rational design of the metalens structure, such as couple nanorods, and stacking or stitching several layers of metasurfaces.

4 Conclusions

To conclude, we demonstrate the design of a metalens based on the AlN nanorod metasurface at the broadband UV region. The in-plane on-axis and off-axis, and out-of-plane focusing characteristics have been investigated for the representative UVA (375 nm), UVB (308 nm) and UVC (244 nm). The corresponding focusing efficiency for UV-375 nm incidence is around 47.09%, 45.82% and 44.96%, respectively. UV routers for mono-wavelength and multiple wavelengths have been designed further, with the routing efficiency to be 12.4% (244 nm), 18.6% (first quadrant), 18.0% (third quadrant) and 7.17% (375 nm), respectively, for the demonstrated square image routing. The crosstalk effect has been discussed and can be reduced by further optimized structure design to decrease the conversion spectrum overlap between different building blocks. The designed UV metalens and UV router should have application in UV directional light, laser, lithography, communication and sterilization, image sensor and so on, and our work would promote the development of miniaturization and high-density integration of the UV nanophotonics.

Acknowledgments: This work was supported by National Key Research and Development Program of China (2018YFB0406702), the Professorship Start-up Funding (No. 217056), Innovation-Driven Project of Central South University (No. 2018CX001), Project of State Key Laboratory of High Performance Complex Manufacturing, Central South University (No. ZZYJKT2018-01), and Guangzhou Science & Technology Project of Guangdong Province, China (201704030106 and 2016201604030035).

References

[1] Yu N, Capasso F. Flat optics with designer metasurfaces. Nature Mater 2014;13:139–50.
[2] Arbabi A, Horie Y, Bagheri M, Faraon A. Dielectric metasurfaces for complete control of phase and polarization with subwavelength spatial resolution and high transmission. Nat Nanotechnol 2015;10:937–43.
[3] Jahani S, Jacob Z. All-dielectric metamaterials. Nat Nanotechnol 2016;11:23–36.
[4] Pors A, Nielsen MG, Bozhevolnyi SI. Broadband plasmonic half-wave plates in reflection. Opt Lett 2013;38:513–5.
[5] Fattal D, Li J, Peng Z, Fiorentino M, Beausoleil RG. Flat dielectric grating reflectors with focusing abilities. Nat Photonics 2010;4:466–70.
[6] Khorasaninejad M, Chen WT, Zhu AY, et al. Multispectral chiral imaging with a meta-lens. Nano Lett 2016;16:4595–600.
[7] Khorasaninejad M, Chen WT, Devlin RC, Oh J, Zhu AY, Capasso F. Metalenses at visible wavelengths: diffraction-limited focusing and subwavelength resolution imaging. Science 2016;352:1190–4.
[8] Schonbrun E, Seo K, Crozier KB. Reconfigurable imaging systems using elliptical nanowires. Nano Lett 2011;11:4299–303.
[9] Avayu O, Almeida E, Prior Y, Ellenbogen T. Composite functional metasurfaces for multispectral achromatic optics. Nat Commun 2017;8:14992.
[10] Eisenbach O, Avayu O, Ditcovski R, Ellenbogen T. Metasurfaces based dual wavelength diffractive lenses. Opt Express 2015;23:3928–36.

[11] Wang SM, Wu PC, Su V-C, et al. Broadband achromatic optical metasurface devices. Nat Commun 2017;8:187.
[12] Huang K, Dong Z, Mei S, et al. Silicon multi-meta-holograms for the broadband visible light. Laser Photonics Rev 2016;10:500–9.
[13] Zheng G, Mühlenbernd H, Kenney M, Li G, Zentgraf T, Zhang S. Metasurface holograms reaching 80% efficiency. Nat Nanotechnol 2015;10:308–12.
[14] Chen WT, Yang K-Y, Wang CM, et al. High-efficiency broadband meta-hologram with polarization-controlled dual images. Nano Lett 2014;14:225–30.
[15] Huang YW, Chen WT, Tsai WY, et al. Aluminum plasmonic multicolor meta-hologram. Nano Lett 2015;15:3122–7.
[16] Khorasaninejad M, Ambrosio A, Kanhaiya P, Capasso F. Broadband and chiral binary dielectric meta-holograms. Sci Adv 2016;2:e1501258.
[17] Wang B, Dong F, Li QT, et al. Visible-frequency dielectric metasurfaces for multiwavelength achromatic and highly dispersive holograms. Nano Lett 2016;16:5235–40.
[18] Zhao W, Liu B, Jiang H, Song J, Pei Y, Jiang YY. Full-color hologram using spatial multiplexing of dielectric metasurface. Opt Lett 2016;41:147–50.
[19] Li QT, Dong FL, Wang B, et al. Polarization-independent and high-efficiency dielectric metasurfaces for visible light. Opt Express 2016;24:16309–19.
[20] Wang L, Kruk S, Tang HZ, et al. Grayscale transparent metasurface holograms. Optica 2016;3:1504–5.
[21] Proust J, Bedu F, Gallas B, Ozerov I, Bonod N. All-dielectric colored metasurfaces with silicon Mie resonators. ACS Nano 2016;10:7761–7.
[22] Sun S, Zhou Z, Zhang C, et al. All-dielectric full-color printing with TiO2 metasurfaces. ACS Nano 2017;11:4445–52.
[23] Clausen JS, Højlund-Nielsen E, Christiansen AB, et al. Plasmonic metasurfaces for coloration of plastic consumer products. Nano Lett 2014;14:4499–504.
[24] Kumar K, Duan H, Hegde RS, Koh SCW, Wei JN, Yang JKW. Printing colour at the optical diffraction limit. Nat Nanotech 2012;7:557–61.
[25] Miyata M, Hatada H, Takahara J. Full-color subwavelength printing with gap-plasmonic optical antennas. Nano Lett 2016;16:3166–72.
[26] Yokogawa S, Burgos SP, Atwater HA. Plasmonic color filters for CMOS image sensor applications. Nano Lett 2012;12:4349–54.
[27] Xu T, Wu Y-K, Luo X, Guo LJ. Plasmonic nanoresonators for high-resolution colour filtering and spectral imaging. Nat Commun 2010;1:59.
[28] Wu PC, Tsai W-Y, Chen WT, et al. Versatile polarization generation with aluminium plasmonic metasurface. Nano Lett 2017;17:445–52.
[29] Zhao Z, Pu M, Gao H, et al. Multispectral optical metasurfaces enabled by achromatic phase transition. Sci Rep 2015;5:15781.
[30] Pu M, Li X, Ma X, et al. Catenary optics for achromatic generation of perfect optical angular momentum. Sci Adv 2015;1:e1500396.
[31] Wang SM, Wu PC, Su V-C, et al. A broadband achromatic metalens in the visible. Nat Nanotech 2018;13:227–32.
[32] Maguid E, Yulevich I, Yannai M, Kleiner V, Brongersma ML, Hasman E. Multifunctional interleaved geometric-phase dielectric metasurfaces. Light Sci Appl 2018;6:e17027.
[33] Chen WT, Zhu AY, Khorasaninejad M, Shi Z, Sanjeev V, Capasso F. Immersion meta-lenses at visible wavelengths for nanoscale imaging. Nano Lett 2017;17:3188–94.
[34] Chen BH, Wu PC, Su V-C, et al. GaN metalens for pixel-level full-color routing at visible light. Nano Lett 2017;17:6345–52.
[35] Dimitrova VI, Manova DI, Dechev DA. Study of reactive DC magnetron sputtering deposition of AlN thin films. Vacuum 1998;49:193–7.
[36] Liu W, Wang ZW, Yang QD, Liu Y, Wei JT, Tang WQ. Optical properties of Aluminum nitride thin film. J Chin Ceram Soc 2007;35:616–8 + 623.
[37] Anani M, Abid H, Chama Z, Mathieu C, Sayede A, Khelifa B. InxGa1-xN refractive index calculations. Microelectron J 2007;38:262–6.
[38] Natali F, Semond F, Massies J, et al. Correlation between threading dislocation density and the refractive index of AlN grown by molecular-beam epitaxy on Si(111). Appl Phys Lett 2003;82:1386–8.
[39] Brunner D, Angerer H, Bustarret E, et al. Optical constants of epitaxial AlGaN films and their temperature dependence. J Appl Phys 1997;82:5090–6.
[40] Guo LH, Xu SY, Wan RQ, et al. Design of aluminum nitride metalens in the ultraviolet spectrum. J. Nanophoton 2018;12:043513.
[41] Lin D, Fan P, Hasman E, Brongersma ML. Dielectric gradient metasurface optical elements. Science 2014;345:298–302.
[42] Khorasaninejad M, Crozier KB. Silicon nanofin grating as a miniature chirality-distinguishing beam-splitter. Nat Commun 2014;5:5386.
[43] Pancharatnam S. Generalized theory of interference, its applications. Proc Indian Acad Sci A 1956;44:247–62.
[44] Berry MV. The adiabatic phase and Pancharatnam's phase for polarized light. J Mod Optics 1987;34:1401–7.
[45] Chen WT, Zhu AY, Sanjeev V, et al. A broadband achromatic metalens for focusing and imaging in the visible. Nat Nanotech 2018;13:220–6.
[46] Bayer BE. Color imaging array. US patent. US3971065A, 1976.

Supplementary Material: The online version of this article offers supplementary material (https://doi.org/10.1515/nanoph-2018-0151).